ACS APPLIED ELECTRONIC MATERIALS

pubs.acs.org/acsaelm Letter

Temperature-Dependent Phase Stable Hybrid Halide Perovskite Films by Chemical Vapor Deposition

Randy Burns, Siphelo Ngqoloda, Stephen C. Klue, Evguenia Karapetrova, Christopher J. Arendse, and Suchismita Guha*

Cite This: *ACS Appl. Electron. Mater.* 2022, 4, 4258−4264 Read Online

ACCESS | Metrics & More | Article Recommendations

ABSTRACT: Methylammonium lead iodide ($MAPbI_{3-x}Cl_x$) thin films were synthesized using chemical vapor deposition. Temperature-dependent grazing incidence synchrotron-based X-ray diffraction measurements confirm that the structure of $MAPbI_{3-x}Cl_x$, where Cl acts more like a dopant, remains throughout in the tetragonal phase in the temperature range of 20−300 K. These studies are further correlated with temperature-dependent photoluminescence (PL) studies. The PL peak energy monotonically increases with temperature, suggestive of a single-phase behavior. Resistance measurements conducted as a function of temperature show an absence of inflection points, suggesting uniformity in its phase. Between 200 and 325 K, the resistance remains a constant.

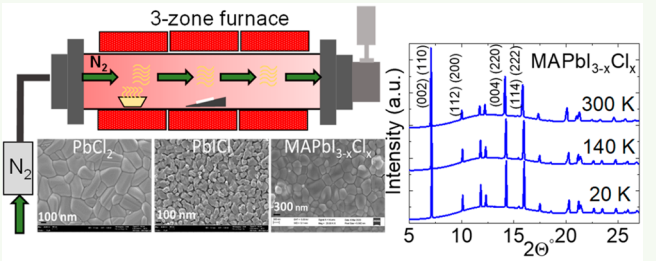

KEYWORDS: *halide perovskite, X-ray diffraction, chemical vapor deposition, electrical transport, thermal stability*

Organic−Inorganic hybrid perovskite (OIHP) materials have radically disrupted the research paradigm of modern photovoltaics in recent years.[1] OIHPs have also attracted applicational interest in terms of near-IR photodetectors and displays,[2] spintronics,[3] and memory devices.[4] These perovskite materials have a unique combination of a high optical absorption coefficient, tunable band gap, ambipolar charge transport, long carrier lifetime, large diffusion length, and the ability to be fabricated using low-temperature processing techniques. Significant research efforts, driven in part by commercial aspirations, have contributed to the drastic increase in the power conversion efficiency for OIHP solar cells from 3% in 2009 to over 25%. However, these perovskite films and crystals unfortunately struggle greatly with stability whenever the film is exposed to heat, light, and moisture. For methylammonium lead iodide ($MAPbI_3$) specifically, a structural phase change from tetragonal (space group (SG) $I4/mcm$) to cubic (SG $pm\bar{3}m$) occurs above 320 K[5−8] which is a temperature well within the standard operational range of a solar cell. Consequently, a solar cell that utilizes $MAPbI_3$ as the semiconductor in the active absorption layer will incur losses in efficiency and longevity as the device fluctuates on the boundary of this phase change during operation.[9] Because hybrid perovskites incur significant ion migration of the halogen atom, minimizing the occurrence of structural phase transitions during operation can help mitigate irreversible diffusion of the halogen atoms and improve long-term stability.

The order−disorder type phase transition in $MAPbX_3$ (X = I, Cl, Br) due to the orientational ordering of the MA^+ ion was predicted almost two decades ago based on calorimetric measurements and infrared vibrational spectroscopy.[7] The organic cations can freely rotate, independent of the PbX_6 octahedra at high temperatures, yielding its cubic symmetry, whereas low temperatures freeze the molecular relaxational degrees of freedom. Based on the antiferro-distortive instabilities observed in oxide perovskites,[10] it was predicted that the tetragonal to cubic structural transition in $MAPbI_3$ results from a condensation of the order parameter fluctuations at the R point of the Brillouin zone.[11] Similarly, the orthorhombic to tetragonal (SG $Pnma$) phase transition at 160 K arises from a condensation of the acoustic modes at the M point (octahedral tilt).[12] The nature of these phase transitions implies that the growth parameters may influence the transition temperature.

Many mechanisms and routes to improve the stability of OIHP solar cells including diffusion barriers, additive engineering, chemically inert electrode optimization, and compositional mixing of the perovskite (formamidinium and halogen mixing) have been investigated. However, the growth method itself plays a significant role in the final performance of the device. There are several published reports detailing the

Received: April 6, 2022
Accepted: June 15, 2022
Published: July 14, 2022

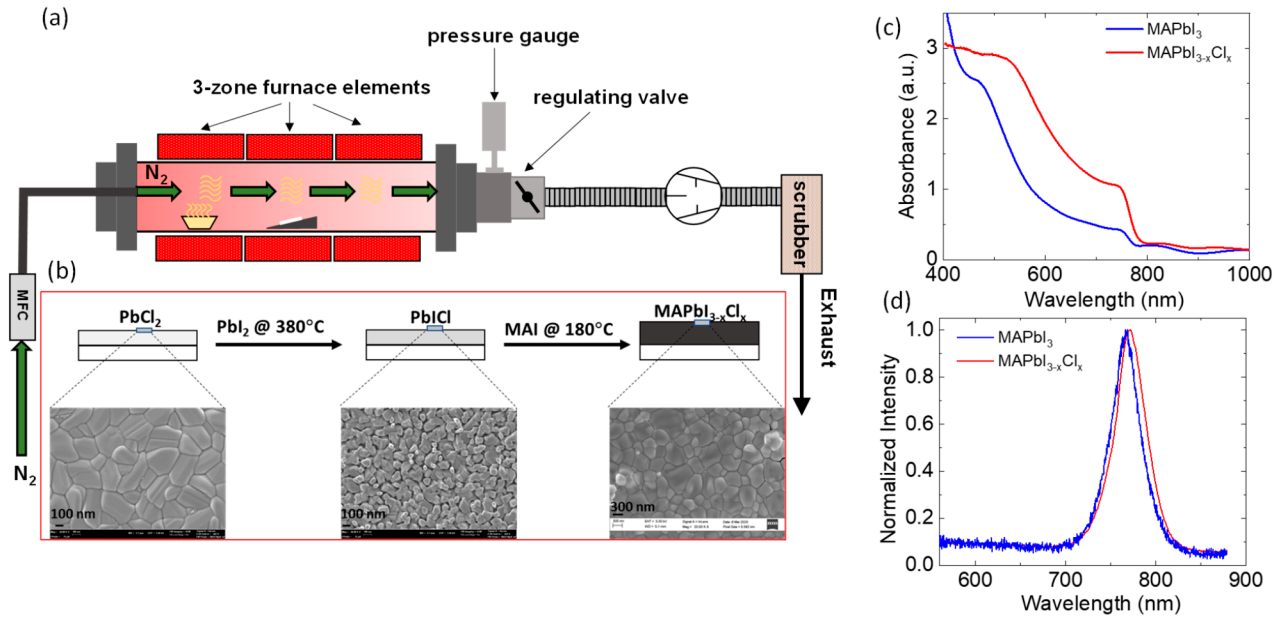

Figure 1. (a) Schematic of the CVD chamber. (b) Three process steps toward the deposition of $MAPbI_{3-x}Cl_x$. SEM images of $PbCl_2$, PbICl, and $MAPbI3_{-x}Cl_x$ films are shown below. (c) Absorption and (d) PL spectra of $MAPbI_3$ and $MAPbI_{3-x}Cl_x$ films at room temperature.

existence of different structural phase diagrams and transition temperatures resulting from divergent entropic conditions of the growth process. In particular, long thermal annealing of compacted $MAPbI_3$ perovskite powder results in the cubic phase at 300 K.[13] Most $MAPbI_3$ films are produced using solution processes such as spin-coating or inkjet printing that, although fast to deposit, produce less stable and robust films compared to other methods. Vapor deposition methods involving either a single step with simultaneous deposition of the organic cation and the metal halide or multistep sequential deposition result in controllable and robust perovskite films. Ngqoloda et al. reported on a simple two-step and low pressure chemical vapor deposition method that produced air stable $MAPbI_3$ thin films which showed excellent power conversion efficiency in solar cells for 21 days without any additional encapsulation or alteration to the perovskite absorption layer.[14] In another work, a three-step vapor deposition using PbSe as the first precursor layer demonstrated $MAPbI_3$ films in the cubic phase under ambient conditions.[15] Here, we highlight the opportunity for vapor deposition growth methods to mitigate some of the intrinsic phase-structure instability exhibited in OIHP materials.

Mixed halide perovskites such as $MAPbI_{3-x}Cl_x$, with long charge carrier diffusion lengths, have been explored in solar cells and have been found to improve stability and hysteresis.[16−19] Using either a two- or three-step chemical vapor deposition (CVD) process, our prior work showed that, in $MAPbI_{3-x}Cl_x$, substitution of chlorine by iodine ions occurred only during the conversion to the perovskite phase, preceded by a stable PbICl phase. No trace of Cl could be detected by energy dispersive X-ray spectroscopy or X-ray photoelectron spectroscopy in the converted perovskite films, suggesting that Cl acts mainly as a dopant in $MAPbI_3$ films.[20] These films, when incorporated in solar cells, showed a higher power conversion efficiency compared with non-Cl $MAPbI_3$ films in addition to high stability to humidity and oxygen exposure. These observations highlight the necessity for detailed investigations of phase transitions and structural behavior induced from less common growth methods such as CVD for the growth of mixed halide perovskite films. Our nomenclature here is such that we refer to Cl incorporated $MAPbI_3$ films as mixed halide ($MAPbI_{3-x}Cl_x$). We present a novel finding using the aforementioned two-step CVD process of $MAPbI_{3-x}Cl_x$ films. Using grazing incidence synchrotron X-ray diffraction (GIXRD), we present a structurally stable $MAPbI_{3-x}Cl_x$ film that remains in the tetragonal phase throughout the range from 20 to 300 K. These results corroborate the temperature-dependent photoluminescence (PL) studies. Additionally, the PL peak position monotonically increases in energy with the absence of discontinuities at any temperature between 20 and 325 K.

The lead(II) iodide powder (PbI_2, purity 99.5%) and lead(II) chloride powder ($PbCl_2$, purity 98%) were purchased from Sigma-Aldrich Inc. Methylammonium iodide (MAI, purity > 99%) was purchased from Dyesol. The perovskite thin films were deposited by sequential low-pressure CVD using a quart tube reactor.[14] Due to the differences in the melting temperature of the precursor materials, a one-step CVD method is quite challenging. The $MAPbI_3$ film and its mixed-halide counterpart with Cl were prepared by a two- and three-step process, respectively.

For $MAPbI_3$ (with no Cl), we used a procedure where a pure PbI_2 layer is deposited at a deposition pressure of 3 mbar on glass substrates 24 cm downstream from the source (ceramic boats containing 36 mg of the PbI_2) as schematically shown in Figure 1a. To improve the thickness uniformity, the substrate holder is usually tilted at an angle of 30° with respect to the direction of the gas flow. The PbI_2 source is vaporized at 380 °C while a 500 sccm N_2 gas flow using a mass flow controller is maintained. The resultant PbI_2 thin films are typically ∼140 nm thick. The Pb-mixed halide thin films were deposited in a similar fashion to that of $MAPbI_3$ in a two-step process. First, a $PbCl_2$ thin film was deposited from a 20 mg $PbCl_2$ source placed in a fresh ceramic boat. With the exception of increasing the vaporization temperature of $PbCl_2$ to 420 °C, the deposition parameters were similar to those of

https://doi.org/10.1021/acsaelm.2c00449
ACS Appl. Electron. Mater. 2022, 4, 4258−4264

the PbI_2 layer. The $PbCl_2$ layer was then subjected to the exact deposition process of the PbI_2 layer. However, 20 mg of PbI_2 source material was used in this step to ensure that the desired 150 nm thickness thin films grew with a PbICl crystal structure.[20] The process is schematically shown in Figure 1b.

The Pb-halide thin films were subsequently and simultaneously converted to the perovskite phase, using a fresh quartz tube. For this step, 150 mg of MAI salt was placed in a fresh ceramic boat that was heated to 180 °C. The Pb-halide films were then positioned 8 cm downstream from the MAI source, with their surface parallel to the gas flow direction (no tilting). The N_2 flow rate was maintained at 100 sccm, resulting in a pressure of 10 mbar. The conversion process was completed after 60 min, which delivered dark brown perovskites thin films.

Grazing incidence temperature-dependent X-ray diffraction (XRD) measurements from 20 to 300 K at an incident angle of 2.9° were performed at sector 33-BM-C, in the Advanced Photon Source (APS) at Argonne National Laboratory.[21] The samples were cooled using the DE-202 cryocooler with a carbon dome from Advanced Research Systems. A microfocused monochromatic X-ray beam (diameter: 100 μm) of wavelength 0.7740 Å was used. The raw data was then analyzed using the FullProf suite, and the lattice parameters were initially refined using the Le Bail method. The pseudo-Voigt function was used to model the peak shapes, and the profile parameters R_b, R_p, R_{wp}, and χ^2 were used as quantitative guides to determine the quality of the resulting fit. Rietveld refinement was used to obtain relative atom positions and bond angles.

A Zeiss Auriga field-emission gun scanning electron microscope (SEM), operated at an acceleration voltage of 5.0 kV, was used to probe the surface morphology of the films. The temperature-dependent PL measurements were carried out in a reflection geometry using a 400 nm diode laser in a closed-cycle helium APD refrigerator. The PL spectra were recorded using an Ocean Optics USB 2000 spectrometer. Two-probe temperature-dependent resistance measurements were conducted under light illumination using a closed-cycle refrigerator with a Keithley 2400 source meter (at 21 V).

The SEM images of $PbCl_2$, PbCl, and $MAPbI_{3-x}Cl_x$ films are shown in Figure 1b. A detailed comparison of the morphology of $MAPbI_{3-x}Cl_x$ with $MAPbI_3$ films is presented in ref 20. In contrast to $MAPbI_3$ films, the average grain size of $MAPbI_{3-x}Cl_x$ is smaller. The smaller grain size was even reflected in PbICl films prior to the conversion by MAI. As reported earlier, the smaller grain size was not detrimental to solar cell performance; on the contrary, the mixed halide perovskites performed better compared to $MAPbI_3$ in solar cells. The optical properties are similar for both $MAPbI_3$ and $MAPbI_{3-x}Cl_x$ as seen from their absorption and PL data in Figure 1c and d. The absorption edge and the PL peak positions are slightly red-shifted for $MAPbI_{3-x}Cl_x$ compared to $MAPbI_3$. We note that neither X-ray photoelectron spectroscopy nor energy dispersive X-ray spectroscopy measurements could detect any signature of Cl in $MAPbI_{3-x}Cl_x$ in our prior work, suggesting that there is no substitution of I by Cl and the Cl ions mainly act as dopants in these films.[20] Similar observations were reported for solution processed perovskites, where no evidence of a $MAPbI_{3-x}Cl_x$ phase was observed.[22] The effects of Cl incorporation in $MAPbI_{3-x}Cl_x$ are evidenced by the improvement in the power conversion efficiency of the solar cell made from this material.[20] Further evidence is a slight red-shift in the PL peak position of this sample compared to $MAPbI_3$ (Figure 1d). This shift further indicates that Cl most likely does not substitute I as that would have resulted in a blue-shift of the energy gap. In order to gauge the impact of Cl on the stability of the perovskite film, we conducted detailed synchrotron-based temperature-dependent GIXRD measurements from a CVD grown $MAPbI_{3-x}Cl_x$ film.

The phase transition from orthorhombic (<160 K) ↔ tetragonal (160−320 K) ↔ cubic (>320 K) perovskite structures in $MAPbI_3$ has been determined by several structural and spectroscopic techniques.[6,8,23] However, insights into structural phase transformation, thus far, have been obtained from either spin-coated films or single crystals. In a prior work, we found that the CVD growth substantially increases the air stability while also inducing the stable cubic phase in $MAPbI_3$ at room temperature and at pressures as low as 0.25 GPa.[24]

Figure 2 displays a stacked GIXRD pattern from a $MAPbI_{3-x}Cl_x$ film at temperature steps of 10 K from 20 to

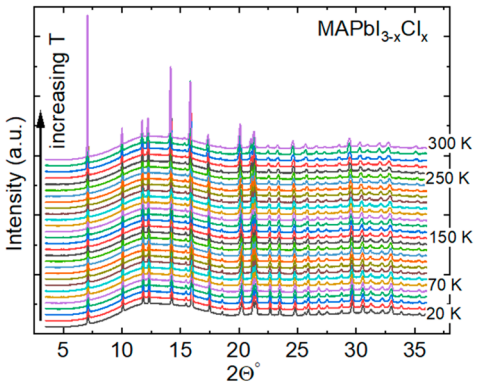

Figure 2. Stacked GIXRD pattern from 20 to 300 K in steps of 10 K from the $MAPbI_{3-x}Cl_x$ film.

300 K. A quick observation highlights that the diffraction pattern undergoes minimal changes in $MAPbI_{3-x}Cl_x$, suggesting a uniform phase across the entire temperature region. This is contrary to what has been observed in $MAPbI_3$, where a distinct structural transformation from the tetragonal to the orthorhombic phase is observed in the range 140−170 K.[8,23]

Figure 3 shows three representative GIXRD patterns at different temperatures along with their Le Bail fits. All three show a similar diffraction pattern with the tetragonal symmetry (SG *I*4/*mcm*), demonstrating a remarkable stability over the temperature range of 20−300 K. The calculated lattice parameters at 300 K are found to be $a = b = 8.900\ (1)$ Å, $c = 12.577\ (5)$ Å, in agreement with other reports of $MAPbI_3$ at 300 K.[5,24] The unique feature here is that, unlike the case of $MAPbI_3$, there is no change to the orthorhombic phase in $MAPbI_{3-x}Cl_x$ at temperatures lower than 160 K. At all temperatures, the sample remains in the tetragonal symmetry. In each case for the fits, the R_{wp} value was less than 5%.

The lattice parameters extracted from the Le Bail fits are seen to increase with temperature, as shown in Figure 4. The structural transitions in $MAPbI_3$ are always accompanied by a stark discontinuity in the lattice constants.[8] The lack of any discontinuity in the lattice parameters and volume (V) in $MAPbI_{3-x}Cl_x$ is consistent with a uniform phase across the temperature range. Since the conventional unit cell of the tetragonal phase contains four formula units, we divide V by 4 in Figure 4 to obtain the variation of the primitive cell volume

https://doi.org/10.1021/acsaelm.2c00449
ACS Appl. Electron. Mater. 2022, 4, 4258−4264

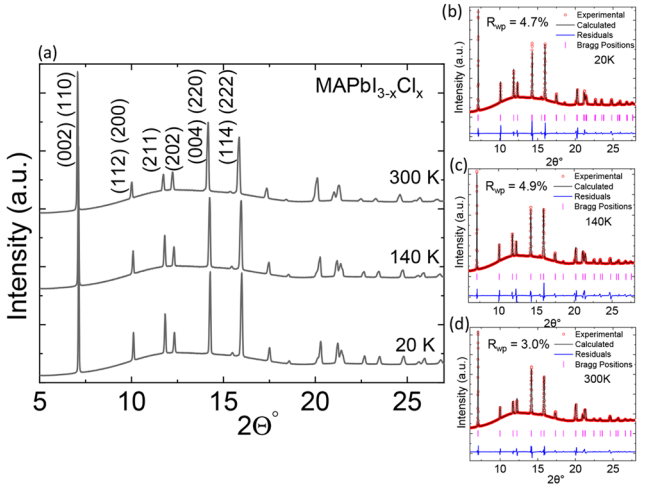

Figure 3. (a) Representative GIXRD pattern for $MAPbI_{3-x}Cl_x$ at three different temperatures with indexed planes. (b–d) Tetragonal ($I4/mcm$) Le Bail fit at 20, 140, and 300 K. The experimental and calculated data are shown as red circles and black line, respectively. The magenta lines denote the Bragg positions, and the blue line is the difference spectrum (residuals).

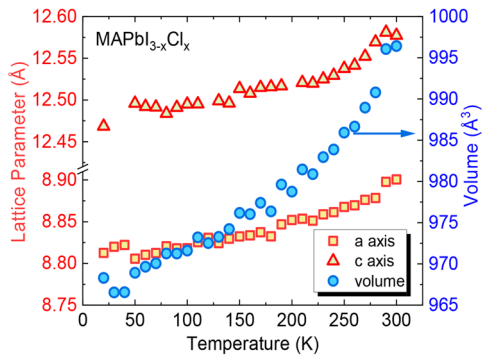

Figure 4. Left axis (square and rectangle) depicts the lattice parameters of $MAPbI_{3-x}Cl_x$ as a function of temperature. Right axis (blue circle) shows the change in volume as a function of temperature.

as a function of temperature. Further, the volume thermal expansion coefficient, given by $\alpha_V = \frac{1}{V}\frac{\partial V}{T}$, where V is the primitive cell volume, may be extracted from the data. We determine $\alpha_V = 1.2 \times 10^{-4}$ K^{-1}, a value similar to what is known for $MAPbI_3$ (1.57×10^{-4} K^{-1}).[25] It should be pointed out that α_V for $MAPbI_{3-x}Cl_x$ is 7 times the value of GaAs and almost 15 times that of Si.[26]

Our findings suggest that the addition of the chlorine halogen ion in the deposition process facilitates a structurally robust film that remains stable from 20 to 300 K. We note that although a detailed structural analysis as a function of temperature has been performed on single crystal and spin-coated $MAPbI_3$ thin films,[8,23,27] similar analyses are sparse in quantity for vapor deposited thin films. The current temperature-dependent GIXRD setup at the beamline (in APS) did not allow for measurements upward of 300 K. It is conceivable that a high temperature cubic phase exists above 300 K in $MAPbI_{3-x}Cl_x$. High temperature GIXRD measurements will be conducted in the future by redesigning the experimental setup.

We note that structural phase transitions in $MAPbI_3$ are strongly dependent on specific growth conditions and entropy configurations. There are few reports which demonstrate the tetragonal to the cubic phase to shift below room temperature in $MAPbI_3$.[13,15,24] Entropy-driven stabilization of the room temperature cubic phase in $MAPbI_3$ was explained on the basis of an entropy increase through the annealing process.[13] For the growth process reported in this work, the addition of Cl atoms substantially increases the number of available microstates due to the distinguishability of the Cl atoms from I which may cause the entropy to rise. Other factors may involve the formation of a small number of Pb–Cl bonds that are stronger than the Pb–I bonds. This, in turn, could weaken the coupling of the organic cation to the ionic bonds present in the octahedral cages and decrease the affinity of the orthorhombic phase to stabilize at all temperatures.

As a check for the uniformity in phase as a function of temperature in CVD grown $MAPbI_{3-x}Cl_x$ films, we have conducted detailed temperature dependent PL and resistance measurements. The PL emission of $MAPbI_{3-x}Cl_x$ is centered at 771 nm at room temperature and slightly red-shifted compared to that of $MAPbI_3$ (Figure 1d). The PL spectra as a function of temperature in Figure 5a show the evolution with a shift to shorter wavelengths with increasing temperatures. The PL spectrum at each temperature was fit with a Lorentzian line shape to obtain the peak energies, full width at half-maximum (fwhm), and intensity; a sample fit at 290 K is shown in the inset of Figure 5b. The PL peak position (in eV) is shown in Figure 5b. The increase in the band gap energy with temperature has been observed in both spin-coated films and single crystals of $MAPbI_3$.[28,29] The changes in the band gap energies in semiconductors arise mainly from two effects: thermal expansion and renormalization of the band energies by electron–phonon interaction. In III–V bulk semiconductors and quantum wells, the electron–phonon interaction is the dominant interaction, which leads to a decrease in the band gap energy with temperature.[30] Since the coefficient of volume expansion in $MAPbI_3$ is at least 10 times higher than that in GaAs, it is this term that plays a dominant role, leading to a net increase in the band gap energy. More recently, scanning tunneling spectroscopic studies have demonstrated an increase in the transport gap with temperature, similar to the optical band gap, and have shed light into the sharp changes at the orthorhombic-tetragonal phase transition in $MAPbI_3$.[27] What is perhaps striking here is that we do not see any evolution of new PL peaks at any temperature, separating the orthorhombic and tetragonal phases, as observed in $MAPbI_3$.[23,28,31] Moreover, we do not see any sharp discontinuity in the PL energy, consistent with our XRD data of a uniform structural phase across the entire temperature range from 20 to 300 K.

The fwhm and the intensity of the PL peak (Figure 5c and d) show some variation with temperature. The fwhm remains a constant until ~200 K and then increases. The peak intensity shows a slight increase at low temperatures and then remains a constant before dropping sharply beyond 200 K. As such, temperature-dependent changes in PL for inorganic semiconductors are a combined effect of exciton–phonon interaction with a renormalization of band energies, thermal expansion, and structural phase transformations, if any. Our XRD data as a function of temperature shows no lattice or volume discontinuities at 200 K, suggesting that the changes observed in the PL at this temperature have a different origin rather than an overall structural phase.

https://doi.org/10.1021/acsaelm.2c00449
ACS Appl. Electron. Mater. 2022, 4, 4258–4264

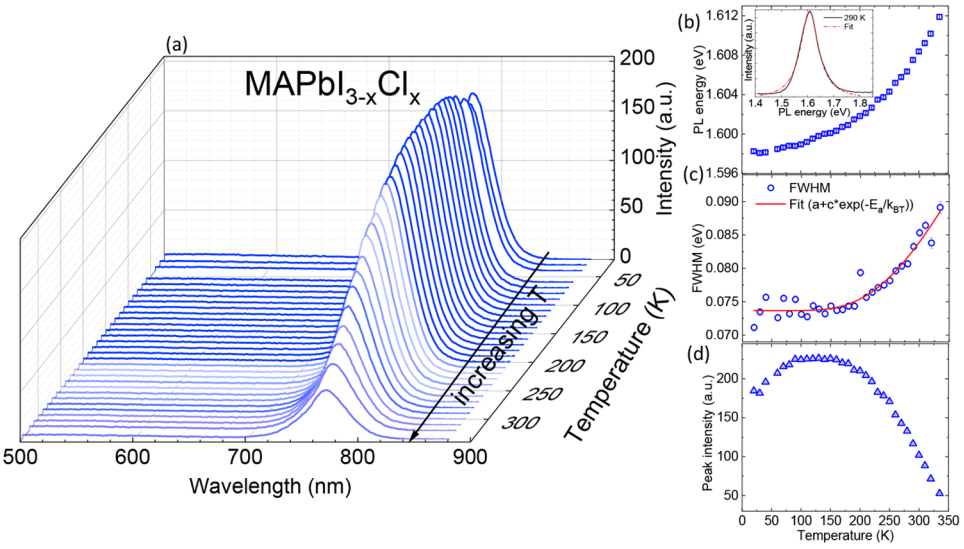

Figure 5. (a) Stacked PL spectra from $MAPbI_{3-x}Cl_x$ at steps of 10 K from 20 to 300 K. (b) Peak PL energies as a function of temperature. The inset shows a fit of the PL spectrum at 290 K to a Lorentzian profile. (c) The fwhm of the PL peak as a function of temperature. The red line is a fit to the equation shown in the legend. (d) PL intensity as a function of temperature.

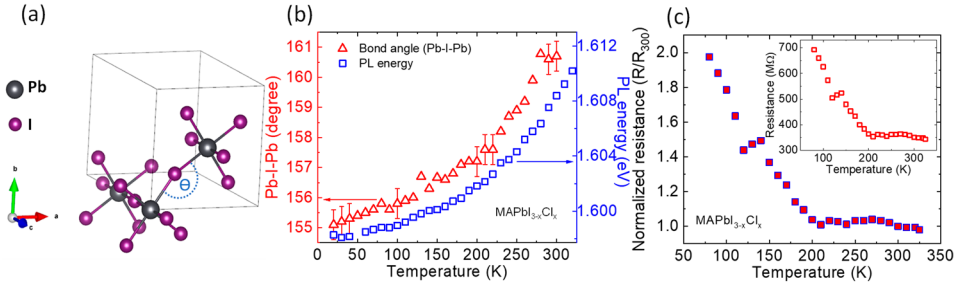

Figure 6. (a) The bond angle of Pb−I−Pb denoted by θ was refined as a function of temperature. (b) Change in the bond angle and the PL energy as a function of temperature. (c) Normalized resistance vs temperature measurements for a $MAPbI_{3-x}Cl_x$ film. The inset plot shows the absolute value of the resistance.

The fwhm was fit with an order−disorder process of the form: $\text{fwhm}(T) = a + c\ \exp\left(-\frac{E_a}{k_B T}\right)$, where a and c are fitting parameters and k_B is the Boltzmann constant; E_a, the activation energy, resembles an exciton−phonon interaction either due to the disorder in the MA unit or in the PbI_6 cage. From the fit, we obtain E_a to be approximately 90 meV. This value is similar to the energy barrier in the disorder of MA cations, as obtained from temperature-dependent Raman scattering in $MAPbBr_3$.[32] Another source could be the tilt and the changes of the bond angles in the PbI_6 cage. Structural Rietveld refinement was conducted in order to obtain the bond angle of the central I atoms to the two closest Pb neighbors. First, preliminary Le Bail fits were made to obtain the lengths of the a, b, and c lattice vectors in addition to the fwhm at each temperature value. The peak shape and heights were refined using a pseudo-Voight function wherein the U, V, and W Caglioti values were optimized. After the Le Bail fits converged to a high quality fit (R_{wp} < 5%), Rietveld analysis was performed on each XRD spectrum for all temperatures using the obtained Le Bail values as a baseline. From the refined atom positions in the Rietveld analysis, the central Pb−I−Pb bond angle was extracted.

Figure 6a shows the dihedral angle of the PbI_6 cage that was tracked as a function of temperature (and plotted using VESTA[33]). As shown in Figure 6b, this angle becomes closer to 180° with the increase in temperature. What is perhaps striking is the similar trend in changes in PL energy and the bond angle with temperature, offering an additional insight into the increasing band gap with temperature. Our results indicate that the change in the Pb−I−Pb bond angle does not, however, affect the overall phase of the sample as determined from XRD. Other changes in the PL fwhm and intensity beyond 200 K can thus be attributed to the change in the bond angle without invoking any change in space group symmetry.

As a further check for the uniformity in phase over temperature, we have carried out resistance measurements as a function of temperature. Transport measurements from $MAPbI_3$ films can be complicated due to the dominance of ionic conductivity over electronic conductivity under dark conditions.[34] In a prior work, we were successful in the synthesis of cubic phase $MAPbI_3$ films (at room temperature) and four-probe resistivity measurements yielded orders of magnitude lower values for resistance compared with $MAPbI_3$ films that are in the tetragonal phase at room temperature.[24] We believe that the occurrence of the cubic phase under ambient conditions could induce some self-doping process due to the presence of local charge defects, similar to what has been observed in $MASnI_3$.[35] More importantly, the trend in the resistance versus temperature showed a one-to-one correlation with the structural phase transitions (at 160 K from

https://doi.org/10.1021/acsaelm.2c00449
ACS Appl. Electron. Mater. 2022, 4, 4258−4264

orthorhombic to the tetragonal phase and at 290 K from the tetragonal to the cubic phase). When $MAPbI_3$ is in the tetragonal phase under ambient conditions, the resistance typically decreases with increasing temperature.[24]

Figure 6c shows the normalized resistance (resistance at a specific temperature/resistance at 300 K) versus temperature from a $MAPbI_{3-x}Cl_x$ film. The inset shows the absolute value of the resistance. The resistance measurements could be tracked upward of 50 K. A decrease in resistance is observed until 200 K, beyond which it remains a constant until 325 K. A semiconductor-metal-like transition has been observed in $MAPbI_3$ near the orthorhombic-tetragonal phase transition,[31] with a continuous decrease in resistance once the sample is in the tetragonal phase. Our results further confirm the presence of the tetragonal phase down to 50 K. The constant value of the resistance beyond 200 K is of special note, because it suggests that the central Pb−I−Pb bond angle change and the tilt of the PbI_6 cage, neither of which alters the total space group symmetry, could be responsible for the behavior of the resistance beyond 200 K.

In summary, the CVD growth of a Cl-doped $MAPbI_{3-x}Cl_x$ film results in a thermally phase-stable crystal structure from 20 to 300 K, as seen from grazing incidence XRD measurements. The film remains throughout in the tetragonal phase (*SG I4/mcm*). The lattice parameters uniformly increase with temperature, and the volume expansion coefficient is obtained as $\alpha_V = 1.2 \times 10^{-4}\ K^{-1}$. The PL results further corroborate the XRD results; no additional PL peaks or any discontinuity are observed at 160 K, signaling the lack of any orthorhombic-tetragonal transition. The increase in the PL energy with temperature is symptomatic of the high α_V compared with III−V semiconductors where the electron−phonon interaction is usually the dominant term. The changes in the PL energy, line width, and intensity are reflective of the planarization of the Pb−I−Pb dihedral angle, even though these changes in the PbI_6 lattice do not affect the overall phase within the temperature range of this study. The resistance shows a continuous decrease until 200 K, beyond which it essentially remains unchanged. CVD growth of Cl incorporated $MAPbI_{3-x}Cl_x$ films thus opens up a path toward phase-stable perovskites, which is expected to be extremely advantageous in the operation of electronic devices.

AUTHOR INFORMATION

Corresponding Author

Suchismita Guha − *Department of Physics and Astronomy, University of Missouri, Columbia, Missouri 65211, United States; Department of Physics and Astronomy, University of the Western Cape, Bellville 7535, South Africa;* orcid.org/0000-0002-6269-2298; Email: guhas@missouri.edu

Authors

Randy Burns − *Department of Physics and Astronomy, University of Missouri, Columbia, Missouri 65211, United States*

Siphelo Ngqoloda − *Department of Physics and Astronomy, University of the Western Cape, Bellville 7535, South Africa*

Stephen C. Klue − *Department of Physics and Astronomy, University of Missouri, Columbia, Missouri 65211, United States*

Evguenia Karapetrova − *Advanced Photon Source, Argonne National Laboratory, Argonne, Illinois 60439, United States*

Christopher J. Arendse − *Department of Physics and Astronomy, University of the Western Cape, Bellville 7535, South Africa; Department of Physics and Astronomy, University of Missouri, Columbia, Missouri 65211, United States;* orcid.org/0000-0002-8505-5320

Complete contact information is available at: https://pubs.acs.org/10.1021/acsaelm.2c00449

Author Contributions

The manuscript was written through contributions of all authors. All authors have given approval to the final version of the manuscript.

Notes

The authors declare no competing financial interest.

ACKNOWLEDGMENTS

We acknowledge the support of this work through the U.S. National Science Foundation (NSF) under Grant No. DMR-1807263. C.J.A. was supported by the South African National Research Foundation (Grant No. 103621, 92520, and 93212) and the Fulbright Research Scholar Program. Use of the Advanced Photon Source was supported by the U.S. Department of Energy, Office of Science, Office of Basic Energy Sciences, under Contract No. DE-AC02-06CH11357.

REFERENCES

(1) Kim, J. Y.; Lee, J.-W.; Jung, H. S.; Shin, H.; Park, N.-G. High-Efficiency Perovskite Solar Cells. *Chem. Rev.* **2020**, *120*, 7867−7918.

(2) Vashishtha, P.; Bishnoi, S.; Li, C. H. A.; Jagadeeswararao, M.; Hooper, T. J. N.; Lohia, N.; Shivarudraiah, S. B.; Ansari, M. S.; Sharma, S. N.; Halpert, J. E. Recent Advancements in near-Infrared Perovskite Light-Emitting Diodes. *ACS Appl. Electron. Mater.* **2020**, *2*, 3470−3490.

(3) Liao, K.; Hu, X.; Cheng, Y.; Yu, Z.; Xue, Y.; Chen, Y.; Gong, Q. Spintronics of Hybrid Organic−Inorganic Perovskites: Miraculous Basis of Integrated Optoelectronic Devices. *Adv. Opt. Mater.* **2019**, *7*, 1900350.

(4) Huang, Y.; Tang, L.; Wang, C.; Fan, H.; Zhao, Z.; Wu, H.; Xu, M.; Shen, R.; Yang, Y.; Bian, J. Triple-Cation Perovskite Resistive Switching Memory with Enhanced Endurance and Retention. *ACS Appl. Electron. Mater.* **2020**, *2*, 3695−3703.

(5) Baikie, T.; Fang, Y.; Kadro, J. M.; Schreyer, M.; Wei, F.; Mhaisalkar, S. G.; Graetzel, M.; White, T. J. Synthesis and Crystal Chemistry of the Hybrid Perovskite (Ch3nh3)Pbi3 for Solid-State Sensitised Solar Cell Applications. *J. Mater. Chem. A* **2013**, *1*, 5628−5641.

(6) Brivio, F.; Frost, J. M.; Skelton, J. M.; Jackson, A. J.; Weber, O. J.; Weller, M. T.; Goñi, A. R.; Leguy, A. M. A.; Barnes, P. R. F.; Walsh, A. Lattice Dynamics and Vibrational Spectra of the Orthorhombic, Tetragonal, and Cubic Phases of Methylammonium Lead Iodide. *Phys. Rev. B* **2015**, *92*, 144308.

(7) Onoda-Yamamuro, N.; Matsuo, T.; Suga, H. Calorimetric and Ir Spectroscopic Studies of Phase Transitions in Methylammonium Trihalogenoplumbates (Ii)†. *J. Phys. Chem. Solids* **1990**, *51*, 1383−1395.

(8) Whitfield, P. S.; Herron, N.; Guise, W. E.; Page, K.; Cheng, Y. Q.; Milas, I.; Crawford, M. K. Structures, Phase Transitions and Tricritical Behavior of the Hybrid Perovskite Methyl Ammonium Lead Iodide. *Sci. Rep.* **2016**, *6*, 35685.

(9) Berhe, T. A.; Su, W.-N.; Chen, C.-H.; Pan, C.-J.; Cheng, J.-H.; Chen, H.-M.; Tsai, M.-C.; Chen, L.-Y.; Dubale, A. A.; Hwang, B.-J. Organometal Halide Perovskite Solar Cells: Degradation and Stability. *Energy Environ. Sci.* **2016**, *9*, 323−356.

(10) Carpenter, M. A. Elastic Anomalies Accompanying Phase Transitions in (Ca,Sr)Tio3 Perovskites: Part I. Landau Theory and a Calibration for Srtio3. *Am. Mineral.* **2007**, *92*, 309−327.

(11) Even, J.; Carignano, M.; Katan, C. Molecular Disorder and Translation/Rotation Coupling in the Plastic Crystal Phase of Hybrid Perovskites. *Nanoscale* **2016**, *8*, 6222−6236.
(12) Beecher, A. N.; Semonin, O. E.; Skelton, J. M.; Frost, J. M.; Terban, M. W.; Zhai, H.; Alatas, A.; Owen, J. S.; Walsh, A.; Billinge, S. J. L. Direct Observation of Dynamic Symmetry Breaking above Room Temperature in Methylammonium Lead Iodide Perovskite. *ACS Energy Lett.* **2016**, *1*, 880−887.
(13) Bonadio, A.; Escanhoela, C. A.; Sabino, F. P.; Sombrio, G.; de Paula, V. G.; Ferreira, F. F.; Janotti, A.; Dalpian, G. M.; Souza, J. A. Entropy-Driven Stabilization of the Cubic Phase of Mapbi3 at Room Temperature. *J. Mater. Chem. A* **2021**, *9*, 1089−1099.
(14) Ngqoloda, S.; Arendse, C. J.; Muller, T. F.; Miceli, P. F.; Guha, S.; Mostert, L.; Oliphant, C. J. Air-Stable Hybrid Perovskite Solar Cell by Sequential Vapor Deposition in a Single Reactor. *ACS Applied Energy Materials* **2020**, *3*, 2350−2359.
(15) Qiu, J.; McDowell, L. L.; Shi, Z. Room-Temperature Cubic Perovskite Thin Films by Three-Step All-Vapor Conversion from Pbse to Mapbi3. *Cryst. Growth Des.* **2019**, *19*, 2001−2009.
(16) Ono, L. K.; Juarez-Perez, E. J.; Qi, Y. Progress on Perovskite Materials and Solar Cells with Mixed Cations and Halide Anions. *ACS Appl. Mater. Interfaces* **2017**, *9*, 30197−30246.
(17) Isikgor, F. H.; Li, B.; Zhu, H.; Xu, Q.; Ouyang, J. High Performance Planar Perovskite Solar Cells with a Perovskite of Mixed Organic Cations and Mixed Halides, Ma1−Xfaxpbi3−Ycly. *J. Mater. Chem. A* **2016**, *4*, 12543−12553.
(18) Heo, J. H.; Lee, M. H.; Jang, M. H.; Im, S. H. Highly Efficient Ch3nh3pbi3−Xclx Mixed Halide Perovskite Solar Cells Prepared by Re-Dissolution and Crystal Grain Growth Via Spray Coating. *J. Mater. Chem. A* **2016**, *4*, 17636−17642.
(19) Tavakoli, M. M.; Gu, L.; Gao, Y.; Reckmeier, C.; He, J.; Rogach, A. L.; Yao, Y.; Fan, Z. Fabrication of Efficient Planar Perovskite Solar Cells Using a One-Step Chemical Vapor Deposition Method. *Sci. Rep.* **2015**, *5*, 14083.
(20) Ngqoloda, S.; Arendse, C. J.; Guha, S.; Muller, T. F.; Klue, S. C.; Magubane, S. S.; Oliphant, C. J. Mixed-Halide Perovskites Solar Cells through Pbicl and Pbcl2 Precursor Films by Sequential Chemical Vapor Deposition. *Sol. Energy* **2021**, *215*, 179−188.
(21) Karapetrova, E.; Ice, G.; Tischler, J.; Hong, H.; Zschack, P. Design and Performance of the 33-Bm Beamline at the Advanced Photon Source. *Nucl. Instrum. Methods Phys. Res.* **2011**, *649*, 52−54.
(22) Fan, L.; Ding, Y.; Luo, J.; Shi, B.; Yao, X.; Wei, C.; Zhang, D.; Wang, G.; Sheng, Y.; Chen, Y.; Hagfeldt, A.; Zhao, Y.; Zhang, X. Elucidating the Role of Chlorine in Perovskite Solar Cells. *J. Mater. Chem. A* **2017**, *5*, 7423−7432.
(23) Osherov, A.; Hutter, E. M.; Galkowski, K.; Brenes, R.; Maude, D. K.; Nicholas, R. J.; Plochocka, P.; Bulović, V.; Savenije, T. J.; Stranks, S. D. The Impact of Phase Retention on the Structural and Optoelectronic Properties of Metal Halide Perovskites. *Adv. Mater.* **2016**, *28*, 10757−10763.
(24) Burns, R.; Ngqoloda, S.; Arendse, C. J.; Lavina, B.; Dahal, A.; Singh, D. K.; Guha, S. Probing Structure−Property Relationship in Chemical Vapor Deposited Hybrid Perovskites by Pressure and Temperature. *J. Mater. Res.* **2021**, *36*, 1805−1812.
(25) Jacobsson, T. J.; Schwan, L. J.; Ottosson, M.; Hagfeldt, A.; Edvinsson, T. Determination of Thermal Expansion Coefficients and Locating the Temperature-Induced Phase Transition in Methylammonium Lead Perovskites Using X-Ray Diffraction. *Inorg. Chem.* **2015**, *54*, 10678−10685.
(26) Otfried, M. *Semiconductors: Basic Data.*; Springer-Verlag: 1996.
(27) Khatun, S.; Maiti, A.; Das, G.; Pal, A. J. Role of Individual Bands in the Unusual Temperature-Dependent Band Gap of Methylammonium Lead Iodide. *J. Phys. Chem. C* **2020**, *124*, 19841−19848.
(28) Singh, S.; Li, C.; Panzer, F.; Narasimhan, K. L.; Graeser, A.; Gujar, T. P.; Köhler, A.; Thelakkat, M.; Huettner, S.; Kabra, D. Effect of Thermal and Structural Disorder on the Electronic Structure of Hybrid Perovskite Semiconductor Ch3nh3pbi3. *J. Phys. Chem. Lett.* **2016**, *7*, 3014−3021.
(29) Fang, H.-H.; Raissa, R.; Abdu-Aguye, M.; Adjokatse, S.; Blake, G. R.; Even, J.; Loi, M. A. Photophysics of Organic−Inorganic Hybrid Lead Iodide Perovskite Single Crystals. *Adv. Funct. Mater.* **2015**, *25*, 2378−2385.
(30) Guha, S.; Cai, Q.; Chandrasekhar, M.; Chandrasekhar, H. R.; Kim, H.; Alvarenga, A. D.; Vogelgesang, R.; Ramdas, A. K.; Melloch, M. R. Photoluminescence of Short-Period Gaas/Alas Superlattices: A Hydrostatic Pressure and Temperature Study. *Phys. Rev. B* **1998**, *58*, 7222−7229.
(31) Campanari, V.; Lucci, M.; Castriotta, L. A.; Paci, B.; Generosi, A.; Guaragno, M.; Francini, R.; Cirillo, M.; Di Carlo, A. Metal-Semiconductor Transition in Thin Film Mapbi3 Perovskite. *Appl. Phys. Lett.* **2020**, *117*, 261901.
(32) Niemann, R. G.; Kontos, A. G.; Palles, D.; Kamitsos, E. I.; Kaltzoglou, A.; Brivio, F.; Falaras, P.; Cameron, P. J. Halogen Effects on Ordering and Bonding of Ch3nh3+ in Ch3nh3pbx3 (X = Cl, Br, I) Hybrid Perovskites: A Vibrational Spectroscopic Study. *J. Phys. Chem. C* **2016**, *120*, 2509−2519.
(33) Momma, K.; Izumi, F. Vesta 3 for Three-Dimensional Visualization of Crystal, Volumetric and Morphology Data. *J. Appl. Crystallogr.* **2011**, *44*, 1272−1276.
(34) Kim, G. Y.; Senocrate, A.; Yang, T.-Y.; Gregori, G.; Grätzel, M.; Maier, J. Large Tunable Photoeffect on Ion Conduction in Halide Perovskites and Implications for Photodecomposition. *Nat. Mater.* **2018**, *17*, 445−449.
(35) Stoumpos, C. C.; Kanatzidis, M. G. The Renaissance of Halide Perovskites and Their Evolution as Emerging Semiconductors. *Acc. Chem. Res.* **2015**, *48*, 2791−2802.

https://doi.org/10.1021/acsaelm.2c00449
ACS Appl. Electron. Mater. 2022, 4, 4258−4264